Unravelling dynamic recrystallisation in a microalloyed steel during rapid high temperature deformation using synchrotron X-rays

Kai Zhang [a,b,c,*], Tim Wigger [a,b], Rosa Pineda [d], Simon A. Hunt [e], Ben Thomas [f], Thomas Kwok [g], David Dye [g], Gorka Plata [h], Jokin Lozares [i], Inaki Hurtado [h], Stefan Michalik [j], Michael Preuss [e,k], Peter D. Lee [a,b,*], Mohammed A. Azeem [l,*]

[a] *Mechanical Engineering, University College London, London, WC1E 7JE, UK*
[b] *Research Complex at Harwell, Harwell Campus, Didcot, OX11 0FA, UK*
[c] *Faculty of Science & Engineering, Swansea University, Bay Campus, Swansea, SA1 8EN, UK*
[d] *Department of Engineering Science and Mathematics, Luleå University of Technology, Luleå, SE 971 87, Sweden*
[e] *Department of Materials, University of Manchester, Manchester, M13 9PL, UK*
[f] *Department of Materials Science and Engineering, University of Sheffield, Sheffield, S10 2TG, UK*
[g] *Department of Materials, Imperial College London, London, SW7 2BP, UK*
[h] *Mechanical and Manufacturing Department, Mondragon Unibertsitatea, Loramendi 4, 20500, Mondragon, Spain*
[i] *Department of Mechanics, Design and Industrial Management, University of Deusto, Avda. de las Universidades 24, 48007, Bilbao, Spain*
[j] *Diamond Light Source Ltd, Harwell Campus, Didcot, OX11 0DE, UK*
[k] *Department of Materials Science and Engineering, Monash University, Clayton, VIC, 3800, Australia*
[l] *School of Engineering, University of Leicester, Leicester, LE1 7RH, UK*

ABSTRACT

Microstructure evolution during high-strain rate and high-temperature thermo-mechanical processing of a 44MnSiV6 microalloyed steel is investigated using *in situ* synchrotron high-energy powder X-ray diffraction. The conditions selected replicate a newly developed near solidus high-strain rate process designed for reducing raw material use during the hot processing of steels. High temperatures (exceeding 1300 °C) and high strain rate $\dot{\varepsilon} = 9$ s^{-1} processing regimes are explored. The lattice strains and dislocation activity estimated from diffraction observations reveal that the microstructure evolution is primarily driven by dynamic recrystallisation. A steady-state stress regime is observed during deformation, which develops due to intermittent and competing work hardening and recovery processes. The texture evolution during the heating, tension, shear deformation and cooling stages is systematically investigated. The direct observation of phase evolution at high-temperature and high-strain rate deformation enables a comprehensive understanding of new manufacturing processes and provides deep insights for the development of constitutive models for face-centred cubic alloys.

1. Introduction

Key industries such as automotive, energy and aerospace sectors rely to a large extent on forging and casting for components and systems. Whilst forging minimises many defects, casting is a low-cost process for manufacturing complex geometries. A newly developed near solidus high-strain rate (NSHSR) processing/manufacturing pathway [1,2] provides the benefits of achieving a forged-like microstructure and simultaneously enables near-net-shape production capabilities. This involves hot processing at 40 °C to 100 °C below the bulk solidus temperature, a temperature regime between forging and conventional semi-solid casting. Feasibility trials for this novel process revealed excellent ductility and malleability on a variety of steel grades, such as 44MnSiV6 microalloyed steel [1,2], resulting in considerable advantages in comparison with conventional forging. For example, about 50% reduction in raw material consumption, a reduced number of processing steps and a significant reduction in equipment operating pressures during manufacturing, are some of the key advantages which help in reducing energy consumption, tool wear and a compact manufacturing footprint [3]. Microalloyed steels are promising materials for this technology, as they achieve excellent mechanical properties and improved strength by adding small amounts of alloying elements [4],

and these steels show one of the highest tensile strengths in their family and they can be tailored to achieve mechanical properties equivalent to that of the quenched and tempered steels, by controlling the hot working processes. However, the microstructural evolution and mechanisms that enable these property improvements at such high temperatures are elusive.

Understanding the temperature pathways, which lead to the formation of optimum grain morphologies and crystallographic texture, is crucial for the accelerated development of metallic alloys in key manufacturing sectors, such as automotive. The texture evolution and intergranular strains can affect the resulting material properties and their distribution in large parts during high throughput net shape production [5–7]. Dynamic recovery and recrystallisation processes have been identified as the most common microstructural mechanisms during the hot working of metals, while dynamic recrystallization (DRX) is regarded as the predominant softening effect in low stacking fault energy materials such as austenitic steels [8–10]. During DRX, a balance between work hardening and recrystallisation is established by the cyclic sequence of events, often composed of tandem build-up of dislocations, grain nucleation at high dislocation density concentrations, followed by grain growth and grain refinement due to the formation of grain boundaries [8]. In NSHSR processing, the temperatures are above the conventional forging temperatures and the strain rates can be high and up to 9 s^{-1} [1,3]. This temperature-pressure working regime has remained unexplored. To date there is no evidence of whether DRX or other mechanisms are operating, and it is still unclear how the observed extreme formability is achieved which enables this unique ability to obtain near net shape components along with a forged-like microstructure.

Often DRX is investigated and quantified from the macro stress-strain response observed during a tension or compression and post-mortem characterisation [11–14]. However, these results do not provide insight into the complex nature of microstructure evolution during the deformation process. This information is sought through *in situ* techniques such as X-ray diffraction which enable a comprehensive understanding of instantaneous microstructures during the deformation process. The direct observation of fast-evolving events such as grain refinement, grain rotation, preferred orientations, lattice strains, dislocation densities and recrystallisation [15], information which is unmatched by any other experimental technique.

There have been several successful investigations using synchrotron X-rays to capture the development of various microstructural features in other systems during thermal and thermo-mechanical processing, such as, dynamic recovery and DRX in Zr [16], phase transitions, dynamic effects and texture in TiAl intermetallics [15], thermally induced phase transitions in shape memory intermetallics [17–19], mosaicity spread in Cu [20], as well as slip and twinning in Mn [21] and steel at ambient temperature [22]. However, these *in situ* thermal mechanical experiments were performed in either compression or tension and at much lower strain rates of 10^{-3} to 10^{-4} s^{-1}. Hence the microstructure evolution observed in such cases cannot be directly used to explain the simultaneous development of forged-like microstructures and the massive metal flow observed in the current novel NSHSR process. Recent advances in X-ray diffraction detector technologies have provided remarkable acquisition speed enhancements, enabling acquisition rates up to 250 Hz [23]. When combined with high flux diffraction optics, they provide ideal instruments for capturing extremely fast evolving microstructures, such as in the case of friction welding [24] and additive manufacturing [25].

In this study, *in situ* high-speed synchrotron X-ray diffraction (XRD) experiments were performed to capture the underlying mechanisms during the NSHSR process. The crystallography, phase changes, the evolution of lattice strains, dislocation activity and texture evolution during processing in a representative Fe system as a function of macro stress-strain response are captured in extensive detail with high temporal resolution. The evolution of material texture and intergranular strains are investigated. The critical stresses and strains for DRX initiation are also evaluated.

2. Experimental methods

### 2.1. Materials and experimental procedures

In situ XRD patterns were acquired at high temperatures during high strain rate tensile and shear deformation of microalloyed 44MnSiV6 steel. The chemical composition of this steel is shown in Supplementary Table 1. This alloy was selected as it is a forging grade and it was used in the full-size component manufacturing trials via the NSHSR forming technique [26]. The alloy has a solidus temperature of $T_S \approx 1394$ °C [26]. The plate from which test specimens were obtained was produced by multiple hot-rolling passes from as-cast material. The hot-rolling was performed at 1100 °C with intermittent annealing for 5 min at the same temperature. This resulted in a microstructure with a grain size of about 10 μm (see Supplementary Fig. 1), which is ideal for power diffraction deformation investigations. "Flat dog-bone" and "lap" specimens with a thickness of 1 mm were designed and manufactured using electro-discharge machining for tensile and shear experiments to represent different deformation modes, respectively (see Fig. 1(a)).

The Electro-Thermo-Mechanical-Tester (ETMT) [27,28], which combines a mechanical loading rig and integrated direct resistive (or "Joule effect") heating, is used in the current investigation. The set-up provides some of the fastest heating and cooling rates during *in situ* X-ray investigations, thus the temperature-pressure conditions observed during NSHSR forming can be mimicked. The specimens were gripped by water-cooled grips inside an environmental chamber with X-ray transparent windows (Fig. 1(b)), providing an inert gas atmosphere to avoid oxidation. The grips are water-cooled and therefore, the maximum and uniform temperature is observed in the middle of the gauge length of the specimen [29]. The incident X-ray beam was aligned with this central region to capture the microstructure evolution.

An R-type thermocouple was spot welded in the central uniform temperature of the gauge length (Fig. 1(b)). The exposure was optimised to achieve a temporal resolution of approximately 100 Hz to capture the fast-evolving microstructure. The load, grip position, heating current and macroscopic stress on the ETMT were recorded with the high frequency of 2000 Hz so that high-frequency diffraction image acquisition can be correlated with the ETMT data. Surface oxidation on the specimens was minimised by purging a constant flow of argon gas (2 l/min) through the enclosed specimen chamber.

To mimic the NSHSR process, each specimen was heated up at a constant rate of 10 °C/s to a target temperature of around 70 to 100 °C below the solidus, reaching 1300 °C to 1330 °C. The specimens were then held at this temperature for 5 s in load control at ~2 N, and then loaded to failure. Either tensile or shear deformation was induced in the central region of the specimen depending on the specimen type. Crosshead velocities of 15 mm/s and 45 mm/s were used for different strain rates of 3 s^{-1} and 9 s^{-1}. Assuming the deformation only occurred in the hot zone along the central gauge length of 5 mm in the tensile specimens and on 5 mm width in the shear specimens, thus strain rates of 3 s^{-1} to 9 s^{-1} were reached in each of the two loading modes depending on the velocity. The specimens were immediately cooled down to room temperature (within 5 s) after the deformation to failure. The stress-strain curves were smoothed using a moving average.

Synchrotron X-rays have sufficient photon flux to record diffraction patterns at high frequencies during high-strain rate deformation tests. The current experiments were conducted at the high energy I12-JEEP beamline [30] at the Diamond Light Source. The ETMT was placed on a translation stage in the experimental hutch, positioning the central region of the specimen in line with the X-ray beam path (red line) and a PILATUS3 X CdTe 2 M area detector [23] (Fig. 1(c)). Monochromatic X-rays with an energy of 89.5 keV ($\lambda = 0.139$ Å) and a beam size of 1×1 mm^2 were used during the heating, deformation and unloading stages.
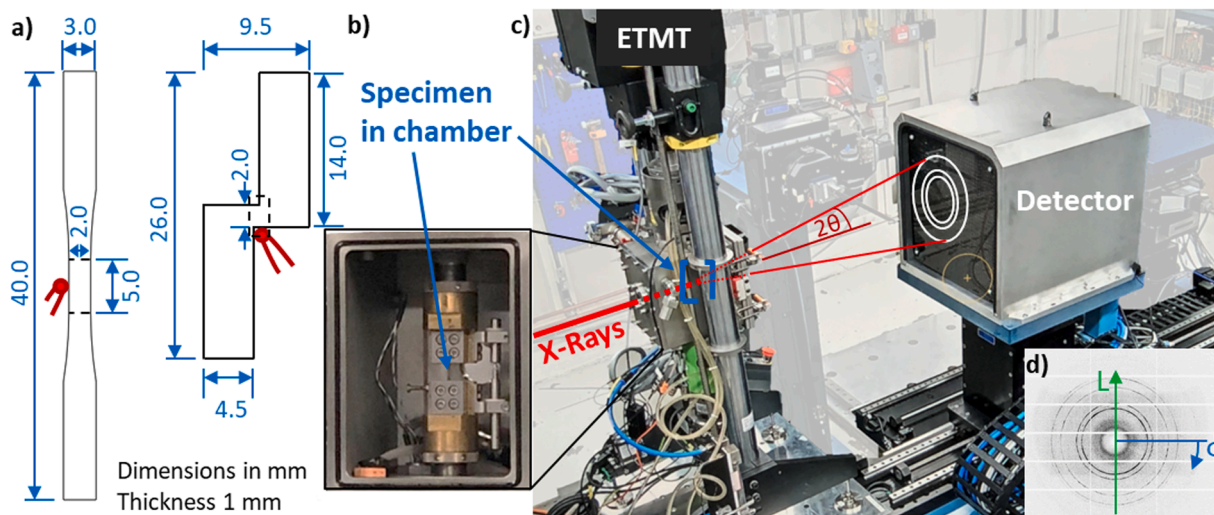
Fig. 1. (a) Schematic of the geometries of dog bone tensile and lap shear specimens, with the positions of the spot-welded thermocouples indicated in red, and the tensile and shear region marked with dashed lines. (b) Close-up of the environmental chamber of the Electro-Thermo-Mechanical Tester (ETMT), including specimen held in grips. (c) In situ synchrotron X-ray diffraction experimental set up at the I12 beamline at Diamond Light Source and (d) Complete Debye-Scherrer (Schematic of a typical diffraction) pattern obtained at room temperature, L is the load direction ϕ is the azimuth angle.

Complete Debye-Scherrer powder diffraction patterns on an area of 1475×1679 pixels and a pixel size of 172×172 μm were obtained. A detector to specimen distance of approximately 650 mm was used and the detector was calibrated using a CeO_2 standard. Complete Debye-Scherrer patterns were acquired up to a diffraction angle (2θ) of $10°$ An exposure time of 3 ms and imaging frequency of 167 Hz was used to ensure the capturing of sufficient frames during the short deformation period of 80 to 200 ms.
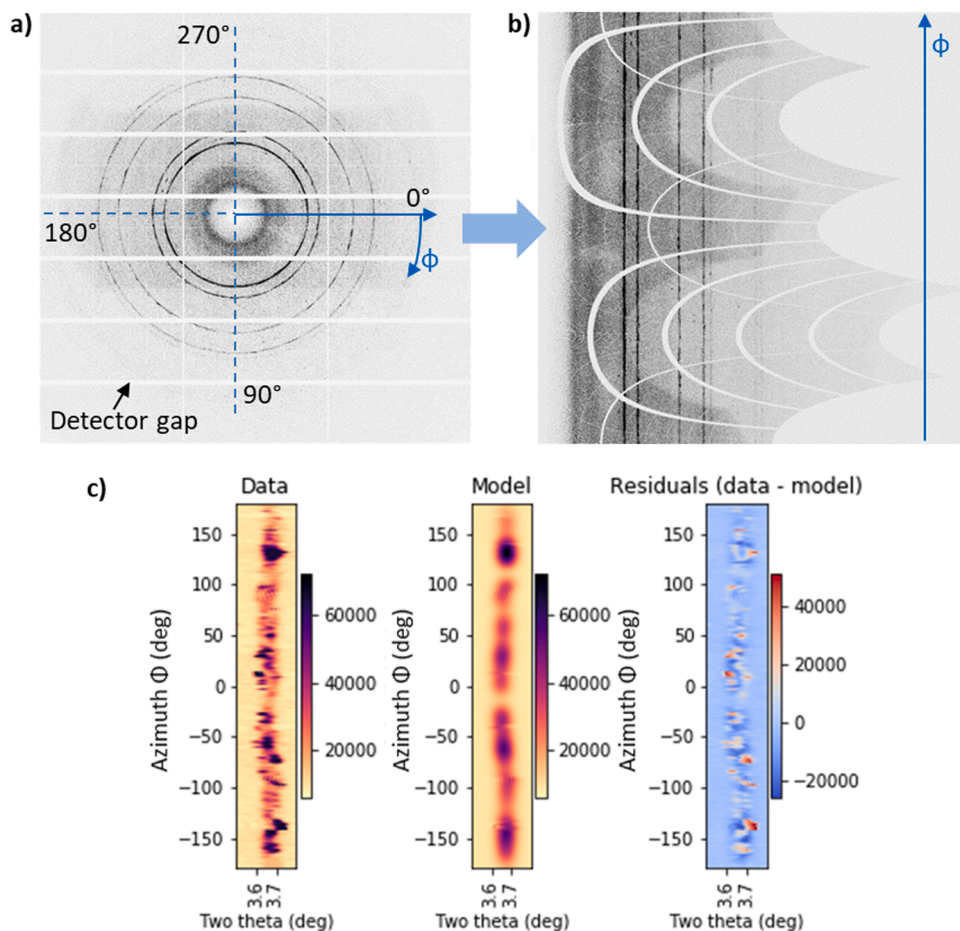
Fig. 2. Principle of CPF by caking a diffraction ring pattern (a) into straight lines (b). An example of a Fourier model generated by CPF is shown in (c), in comparison with experimental data and including a map of the residuals.

2.2. Analysis methods

The intensity of the XRD patterns was first integrated across the azimuth along the entire 360° to generate spectra of the intensity *versus* the diffraction angle 2θ using the DAWN software package [31,32]. The spectra were then examined for the phase composition and background pattern changes to check if there was a liquid formed during the severe deformation process. The material texture was determined using MAUD by averaging over 5 ° [33] and Beartex for visualisation [34]. Due to the very short deformation time, the texture changes were measured and tracked with only one sample orientation.

The data acquisition was optimised to obtain maximum information from the very short duration over which the deformation lasts during high strain rate deformation. The diffraction from the initial room-temperature as rolled sample comprised of complete rings, as shown in Fig. 2(a). However, as temperature exceeded 900 °C during rapid heating, the grains started to coarsen remarkably quickly, resulting in increasingly spotty patterns.

The lack of continuity along the azimuth due to spotty patterns during heating meant that the classical Rietveld analysis approach with function fitting to caked peaks along azimuth could not be used in the current quantification of microstructure evolution. In order to overcome this issue, Continuous Peak Fitting (CPF) [25,35], a novel Fourier function-based technique which fits each complete Debye ring in a single step without resampling or caking the diffraction data, was used. Firstly, the diffraction patterns were de-noised using DAWN [32]. The fitting algorithm tends to weigh the azimuthal function towards the most intense peaks, the image intensity was normalised using DAWN to reduce this effect for the determination of *d*-spacings. The intensity scatter along the azimuth is shown in Fig. 2(b), the diffraction lines are straight across the entire azimuth range, which is a clear indication that there are no residual strains in the as hot-rolled alloys.

Continuous peak fit uses the Fourier series to describe the azimuthal dependency for each of the parameters of a pseudo-voigt peak (height, width, centroid, profile). The order of the Fourier series is determined by the data. The profile and width are 0th order Fourier series (1 parameter for all azimuths) and the peak height is a 6th or 12th order series (13 or 15 terms) depending on the data. The centroid or *d*-spacing of the peak is 2nd order series (5 coefficients). The data fit in that within a narrow 2θ-range around each diffraction peak, as shown in Fig. 2(c). Although this function is still biased towards the brightest spots in the diffraction rings, the continuity of the function and the capped intensities reduce the weighting relative to the traditional way of fitting independent peaks to the resampled and caked data. The magnitude and orientation of the differential strains are calculated from the differential strain coefficients. The errors in these terms are calculated from the coefficient errors without accounting for any correlation between the two parameters [17,36].

The relative change in diffraction peak width for each pattern, which is indicative of the dislocation density occurring during the deformation process [37] can also be measured using CPF. This will allow for the estimation of change in dislocation densities as a function of thermal or thermo-mechanical deformation.

3. Results and discussion

3.1. Macro stress-strain behaviour

Three *in situ* experiments on 44MnSiV6 steel were performed under different conditions; E1: Tensile deformation at 1100 °C and 3 s^{-1}, E2: tensile deformation at 1300 °C and 9 s^{-1} and E3: shear deformation at 1330 °C and 9 s^{-1}. The engineering stress-strain response as acquired on the ETMT during tensile and shear experiments are shown in Fig. 3(a). The strains were calculated assuming a 5 mm central region of the sample, which is the hottest region with almost uniform temperature along the gauge length. The 5 mm shear width was estimated from the
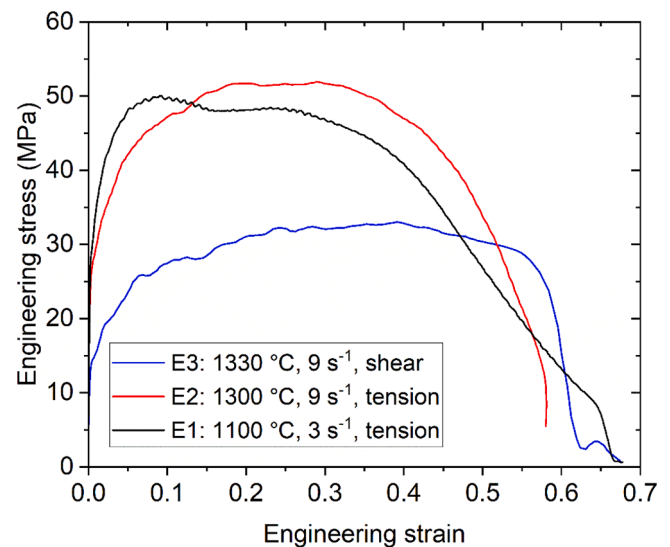

Fig. 3. Engineering-Stress-Strain curves of 44MnSiV6 steel undergoing tensile deformation at 1100 °C and a lower strain rate of 3 s^{-1} (black), tensile deformation at 1300 °C and a higher strain rate of 9 s^{-1} (red), shear deformation at 1330 °C and 9 s^{-1} (blue).

width of the actually deformed region of the specimen.

The engineering stress-strain response shows a typical initial elastic regime followed by plastic deformation. During tensile deformation, the yield strength during tension and shear deformation is observed to be 27 MPa and 14 MPa respectively. The ultimate tensile strength ($\sigma_{1100, 3}$) in E1, was found to be 50 MPa, following which there was plateauing at 48 MPa. After about 30% far-field strain, the stress starts to drop due to localization of deformation followed by failure. A similar stress-strain response is observed during tensile deformation at a higher temperature, E2. This far-field stress-strain response is typical of a system where DRX occurs during thermo-mechanical processes, such as those observed in steels [38], zircaloy [39] and nickel base superalloys [40]. In shear mode, the yield and tensile stress were found to be 14 and 30 MPa respectively with a constant stress deformation between 30 and 40% plastic deformation.

In all three cases, after the elastic regime some initial work hardening was observed that is most likely due to the introduction of dislocations. After some deformation there seems to be simultaneous softening due to recrystallization and recovery, which tends to lower the flow stress and enhance the ductility. The (nearly) constant stress state observed in the plastic regime is thus an indication that there is a competition between stress relaxation due to new grain nucleation and growth and work hardening due to plastic deformation. Similar behaviour is observed during high strain rate deformation of other steels [11,13,41,42] and AZ31 magnesium alloys [43], owing to DRX. According to an estimation method provided in [42] for DRX in a microalloyed steel, the hot section of the specimen fully recrystallizes during late stages of deformation. This dependence of macro stress-strain response on critical initiation points and DRX is crucial for the development of more accurate material and processing models. The peak stress in both tensile experiments is observed to be ~50 MPa, this is owing to the fact that the recrystallization rates are higher at higher temperatures and decrease with strain rate [44]. As expected, in comparison to the peak tensile stress, the peak stress for shear deformation is lower, around 30 MPa.

The key aspects for modelling DRX behaviour are the critical stress and strain at DRX initiation. After passing the elastic limit at the beginning of the deformation process, the dislocation density increases until a critical point is reached, where the first recrystallised nuclei are formed and thus the initiation of DRX [44]. This critical stress and strain for DRX initiation can be determined from the change in strain

hardening rate $\theta = \partial\sigma/\partial\varepsilon$ from plastic to nearly perfectly plastic deformation [45] observed in the stress-strain response. The critical stresses and strains for the present thermo-mechanical scenarios are provided in Table 1, and the strains are rounded to two decimal places. Derivatives of the true stress-strain curves with inflection points during the shear test at 1330 °C, and tension tests at 1300 °C and 1100 °C are plotted in Supplementary Fig. 2. The strain hardening rate decreases with true stress.

3.2. Typical microstructure evolution

The microstructure evolution in the case of E2 is shown in Fig. 4. Initially, the actuator position (red line) is flat, whilst the temperature (black line) remains at approximately 1300 °C, slightly fluctuating due to instrument control response. Only a few diffraction spots per ring are observed (Fig. 4(a)), which is an indication that only a few large grains exist after coarsening in the diffracting sample volume. With the start of deformation (at time 0.00), the temperature increases slightly, most likely due to improved electrical contact and then remains steady. As the deformation progresses, the number of diffraction spots increases (Fig. 4 (b-c)), this is followed by the blurring of spots and then spread along the azimuth (Fig. 4(d)), eventually merging into uniform complete rings which remain intact during further plastic deformation (Fig. 4(e)). During the last third of deformation, at around 0.07 s the temperature increases rapidly to ≈1345 °C. At around 0.09 s, the sample starts to cool which occurs due to an open loop in the ETMT resistance heating circuit, indicating specimen failure. The diffraction patterns gradually turn to spotty during cooling, the final pattern is shown in Fig. 4(f). Towards the end of deformation at around 0.07 s, the temperature rises rapidly, whilst the electrical heating current drops at a similar rate (see Supplementary Fig. 3). This is identified as an effect of necking in the specimen, the reduced cross-section leads to an increase in electrical resistance.

3.3. Evolution of diffraction patterns during deformation

Observing the evolution of diffraction patterns during the tensile and shear experiments would provide lattice and crystallographic insights which can be used to inform existing models or for building new mechanistic models. At first, the diffraction patterns were azimuthally integrated over 360° to obtain intensity *vs* diffraction angle (2θ) patterns. Due to high signal-to-noise ratio, only the first five austenite peaks, (111), (200), (220), (311) and (222) were examined. The only phase which existed before, during and after deformation was fcc Austenite with $a \approx 3.69$ Å. The 360° azimuth integrated intensity as a function of diffraction angle 2θ over the time is shown in Fig. 5. The background remains unchanged and the peaks are sharp during the heating and deformation process. The existence of spotty diffraction tends to make the peaks appear broader when integrated across 360° azimuths. The corresponding engineering stress and grip position with time are plotted in Fig. 5(b). During the deformation, the engineering stress increases and then decreases with time, and the corresponding diffraction pattern intensity increases and then decreases.

A more detailed and convenient method for examining the diffraction intensity changes with time along a diffraction ring is the Azimuth-Time (AT) plots [15,16]. In Fig. 6, 180° sections of the (200) ring were

plotted as straight lines at each time step, showing the evolution of diffraction intensities along half the ring during deformation for three experiments. As time progresses (from bottom to top in each plot), the intensity variation can be assessed to gather a global perspective of the microstructure evolution. A darker colour indicates a higher intensity and the white intermittent vertical stripes marked with orange blocks are from the gaps in the detector, as seen in Fig. 4(a-f). The load axis (L) is located in the middle of each plot at 90°, and the transverse (T) is across 0° and 180° The change of the macro-stress (blue) and the position (red) during each experiment are shown on the left for comparison. The three selected cases are characterised in the following sections. The diffraction intensity subfigures in Fig. 6(a) and (b-c) are chosen to show the most evidence of these microstructural phenomena, although these gaps are not symmetric to the centre as shown in Fig. 2(a). The corresponding AT plots of the (111) rings are provided in Supplementary Fig. 4.
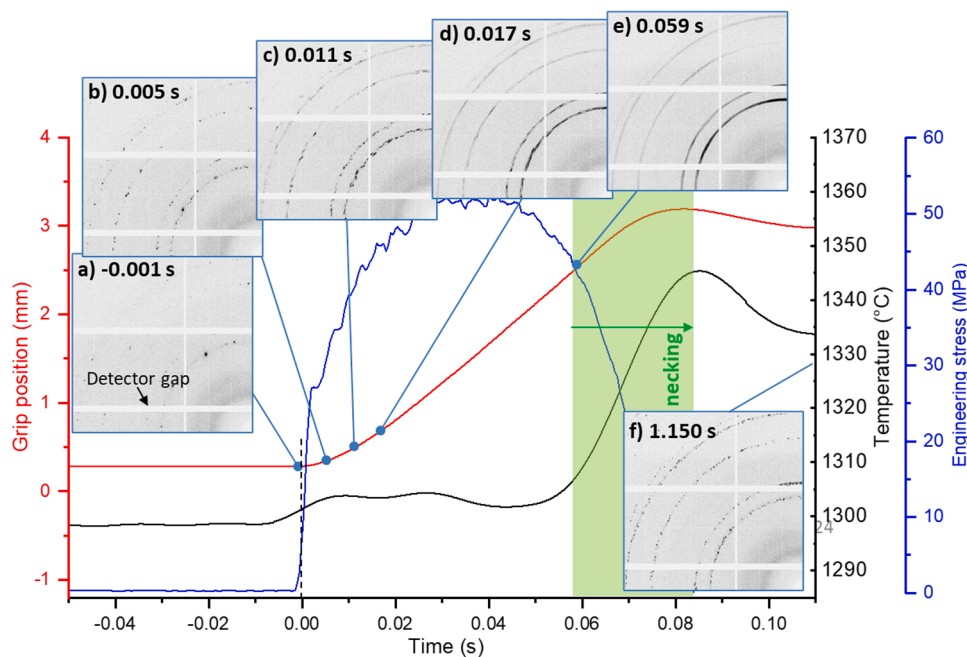
3.3.1. E1: Tensile deformation at 1100 °C and 3 s⁻¹

During low strain rate tensile deformation at 1100 °C, 3 s⁻¹, as shown in Fig. 6(a), we can identify five key stages. In **stage 1**, the existence of a spotty pattern before deformation starts reveals that rapid grain growth has occurred during heating, and the grain size estimated from the diffraction rings can increase from 120 to 150 μm. It has been observed in previous studies that in spite of a steep heating rate, the grain size grows from the initial 10 μm (which results in complete and continuous diffraction rings) at room temperature by nearly 8–10 times at high temperature in Fe base alloy systems [46,47]. Thus the initially complete Deby-Scherrer rings are replaced with a few diffraction spots after heating.

In **stage 2**, at the beginning of deformation (between 0.00 and 0.02 s), diffraction spots appear in several time steps, and during the process, the spotty reflections appear and disappear and increase in number from ~20 to ~40. It is difficult to track these spots as there is no gradual change in location along the ring azimuth for a given spot, this could be due to the grains rotating into and out of the diffracting condition.

During **stage 3**, the diffraction spots start widening and blurring along the azimuth (around 0.025 s). This is caused by the formation of dislocations within the grains, thus dividing the grains into subgrains, and increasing mosaicity and variety in orientations. This process continues generating progressively high-angle grain boundaries which refine the microstructure. Eventually, the reflections merge to form full rings, indicating a reduction in grain size. Several diagonal progressions of intensity profiles, particularly around 60° azimuth (marked with a yellow dashed circle), indicate grain rotation which usually involves slip [20]. The rotation of grains towards the load direction is, however, obscured by the white areas marked with orange blocks which correspond to detector gaps.

In **stage 4**, the deforming material remains in a steady state with mostly homogeneous intensity distribution along the azimuth until 0.13 s, matching the macro-strain plateau as seen in Fig. 6 on the left. Dark "islands" appear and disappear during this state at around 30° and 130 °, in regions marked with D and the red dashed circles. This is a typical observation during DRX [15,16], where such islands are grains with high-angle grain boundaries, nucleating at locations of high dislocation density. These grains subsequently grow and then are refined again by the formation of new dislocations and subgrains. The relatively low strain rate gives the material enough time to form larger grains before decomposing again. Recrystallisation progresses discontinuously across the entire volume, and intermittently in different locations. Firstly, recrystallisation is observed at around 135° after 0.02 s for experiment E1. Dislocations continue to build, and a second recrystallisation activity occurs at ~127°, then the dislocation activity increases again there whilst a third recrystallisation occurs at ~140°, and so forth, as indicated by the red dashed circles in Fig. 6(a). The material hence hardens in some orientations and softens in other orientations at the same time. A curved dark arc is observed at around 160° with periodically increasing

Table 1
Critical strains and stresses for initiation of DRX in 44MnSiV6 during tensile deformation at 1100 °C and 1300 °C, and during shear deformation at 1330 °C (strains are rounded to two decimal places).

DRX initiation in 44MnSiV6	True Strain	True Stress (MPa)
E1	0.04	47.6
E2	0.10	45.1
E3	0.17	31.5

Fig. 4. Evolution of diffraction patterns before (a), during (b-e) and after (f) tensile deformation of 44MnSiV6 microalloyed steel during E2 (1300 °C and at a strain rate of 9 s^{-1}). The sample deformation is clearly identifiable from the increase in grip position (red line) from 0 s to 0.08 s. The measured temperature is shown as a black line, smoothed using a FFT filter to eliminate high-frequency fluctuations from the controls. The engineering stress is shown as a blue line. Localised necking of the specimen occurs in the last third of the deformation, highlighted in green. (See Supplementary animation 1.).
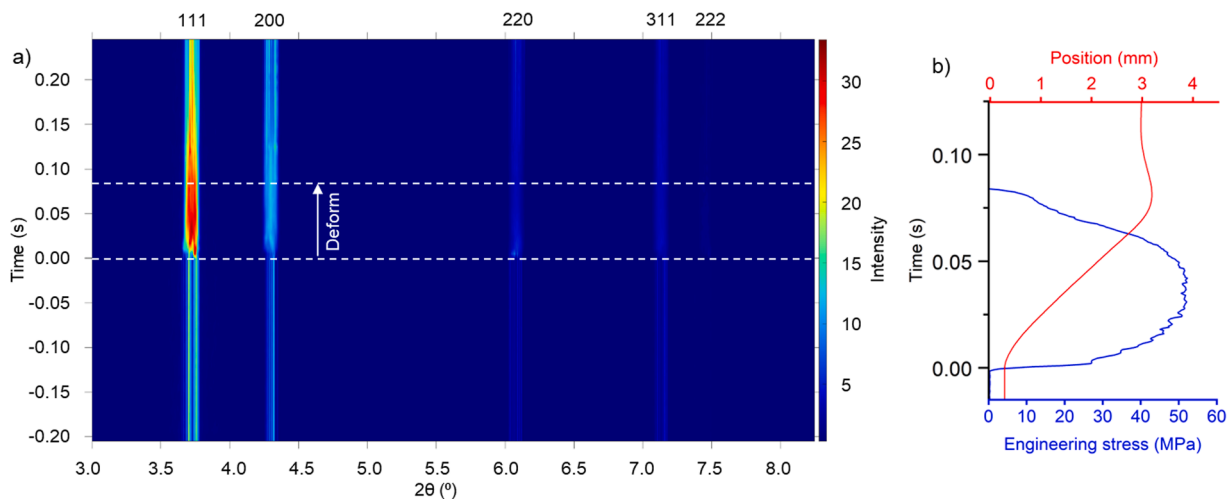
Fig. 5. (a) Evolution of the diffracted intensities with time before, during and after tensile deformation of 44MnSiV6 at 1300 °C, integrated azimuthally over 360° An increase in intensity is evident at the onset of deformation, together with peak broadening. (b) The corresponding engineering stress and grip position with time.

and decreasing intensity (right side of marker A), evidence for subsequent DRX steps with simultaneous rotation [20].

From 0.15 s, **stage 5** starts; the changes observed here are associated with necking in the specimen. Several vertical lines appear in the AT plot at the top of Fig. 6(a), initiated by grain growth during cooling and indicating recovery. This new grain formation during cooling appears at angles which are entirely different to the undeformed state. This phenomenon of new grain formation could be due to the further dynamic recrystallisation during culminating deformation. The specimen fails at 0.23 s and is finally cooled down to room temperature.

3.3.2. E2: Tensile deformation at 1300 °C and 9 s^{-1}

Similar stages are observed in the faster, higher temperature tensile experiment in E2, Fig 6(b). Firstly, massive coarsening is observed

during heating which leads to the formation of spotty patterns from complete Deby-Scherrer rings. Many of these spots vanish and appear during the beginning of deformation between 0.00 s and 0.01 s, their number increases from ~8 to ~25, which is most likely due to recrystallisation early on even though the density of dislocation is expected to be low.

At about 0.01 s after applying the stress, the diffraction spots start to blur due to increasing mosaicity. The steady-state phase here is relatively shorter than in the case of E1 and the recrystallization is not complete, as discussed in Section 3.3. Several small dark DRX islands are observed up to 0.05 s, in regions marked with D. Due to the higher strain rate, relatively less time is available for nucleation, hence the incomplete recrystallisation. It is worth noting that grain rotation, as indicated by diagonal streaks during DRX and necking, is directed towards three
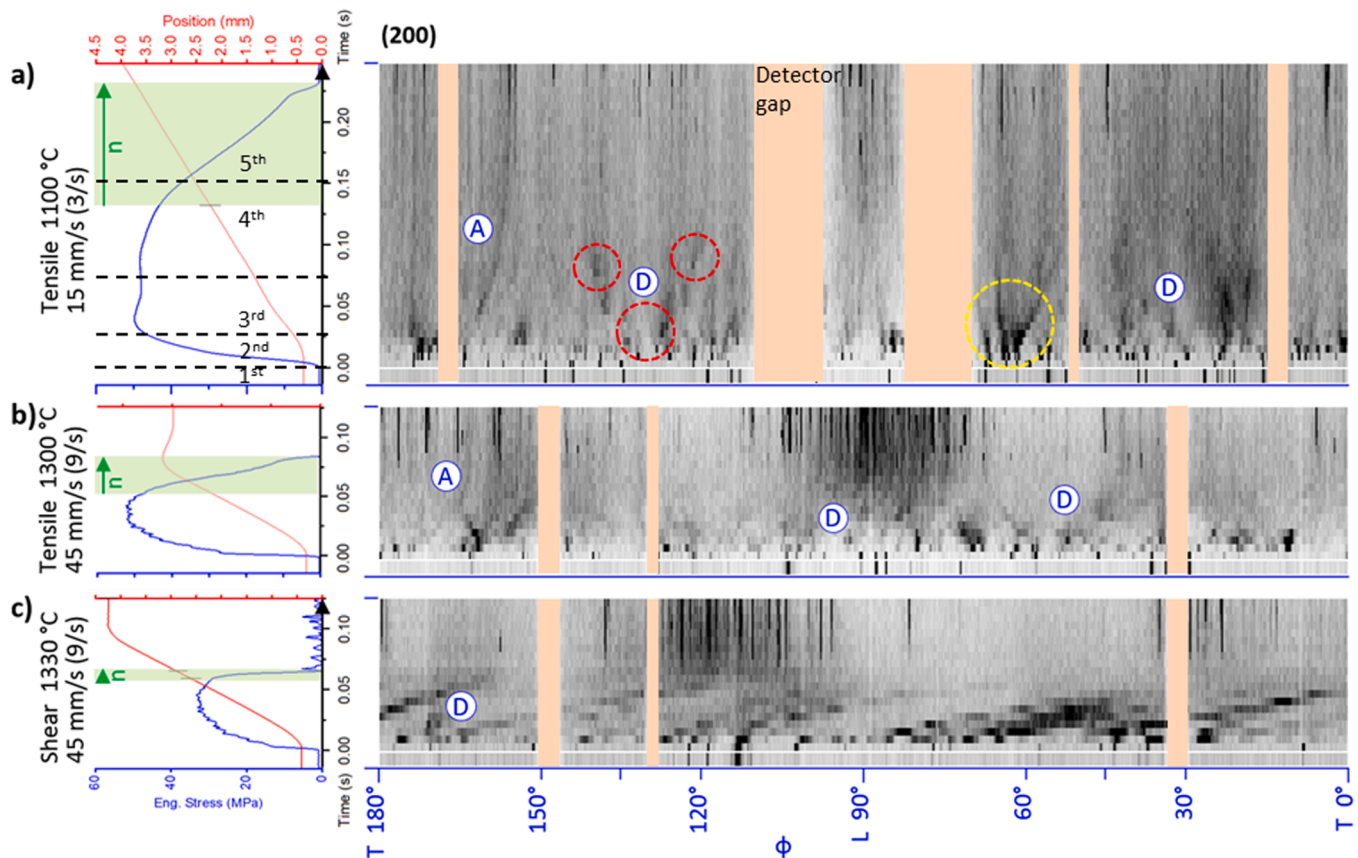
Fig. 6. Diffraction intensity evolution of the (200) ring along 180° of the azimuth over time during (a) the tensile deformation at 1100 °C and 3 s⁻¹, E1, (b) the tensile deformation at 1300 °C and 9 s⁻¹, E2, (c) the shear deformation at 1330 °C and 9 s⁻¹, E3. Time progresses from bottom to top in each plot whilst a darker colour indicates a higher intensity. Regions with DRX-'islands' are annotated with (D), arcs with varying intensity as (A). The white blocks remain from gaps in the detector, as seen in Fig. 4(a-f), and are marked with orange blocks for clarity. The change of macro-stress (blue) and position (red) during each experiment are shown on the left for comparison.

points on the azimuth. Grains rotate predominantly toward the load direction at 90°, creating a "funnel" shape and appear to agglomerate in a dark patch on the AT plot, which is not observed around 30° and 150°. The microstructure analysis of the specimens in the deformed and undeformed zones is conducted with EBSD and SEM (see Supplementary Fig. 5–7). The fracture surface analysis of the specimens is shown in Supplementary Fig. 8.

3.3.3. E3: Shear deformation at 1330 °C and 9 s⁻¹

The AT plot from the shear deformation experiment at 1330 °C shows the same stages, however, with the final funnel-like shape appearing at 120° (Fig. 6(c)), unlike in E2 where it appeared at 90°. The number of diffraction spots increases from initially single digits to approximately 23, as the shear deformation begins at 0.00 s. Darker regions appear during steady-state phases from 0.01 s to 0.06 s and they progress across an incline, indicating rotation of grains in the diffracting volume by about 55° around the sample axis. Some of these may align favourably for slip, hence the significantly lower stresses required for plastic deformation. This may also have induced DRX driving force and faster DRX kinetics than during uniaxial deformation [48]. Although a DRX island might potentially be located near 170°, to the bottom left of marker D, the intense rotation exacerbates the identification of recrystallization features.

Through the deformation stages discussed above, the microstructure still develops with grains nucleating along a specific sample axis, which is evident from the coarsening of grains that leads to the formation of a dark funnel shape in the AT plot in the last phase after 0.07 s. The appearance of this funnel shape in E2 is along the higher azimuth, 115°,

as opposed to 90° in the case of E2.

3.4. Texture evolution

The formation of preferred orientations is investigated by observing the evolution of (111) and (200) rings during heating and deformation, whilst the BCC α-Fe (110) and (200) rings are at around 500 °C and are discussed to highlight the texture formed after phase transformation. Note that the pole figures were reconstructed based on limited information from the diffraction patterns obtained during high-speed deformation. There was no scope to rotate the sample in the very short deformation window that was available due to highly rapid microstructure change. Hence, these orientation diagrams are only provided for gaining qualitative insights into the crystal orientations before, during and after the deformation process.

Fig. 7 shows pole figures obtained during E2 (a-c) and E3 (d-e) respectively from the heating phase before deformation (a, d), during deformation (b, e) and during cooling after deformation (c, f). The loading direction is vertical, as indicated by the black arrows.

During heating, the crystals are randomly orientated and this transforms into a distinct fibre texture during deformation, as high-intensity double bars in 60° steps perpendicular to the vertical load direction in tension (Fig. 7(b)). Such fibres are typical of FCC systems during deformation [49]. Under shear conditions, double bars emerge for the (111) plane and a single bar for the (200) plane, while the pole axis is tilted from the vertical load axis by approximately 23° (Fig. 7(e)). This is likely a result of more new grains nucleating with preferential orientations due to the DRX during the shear process. After deformation
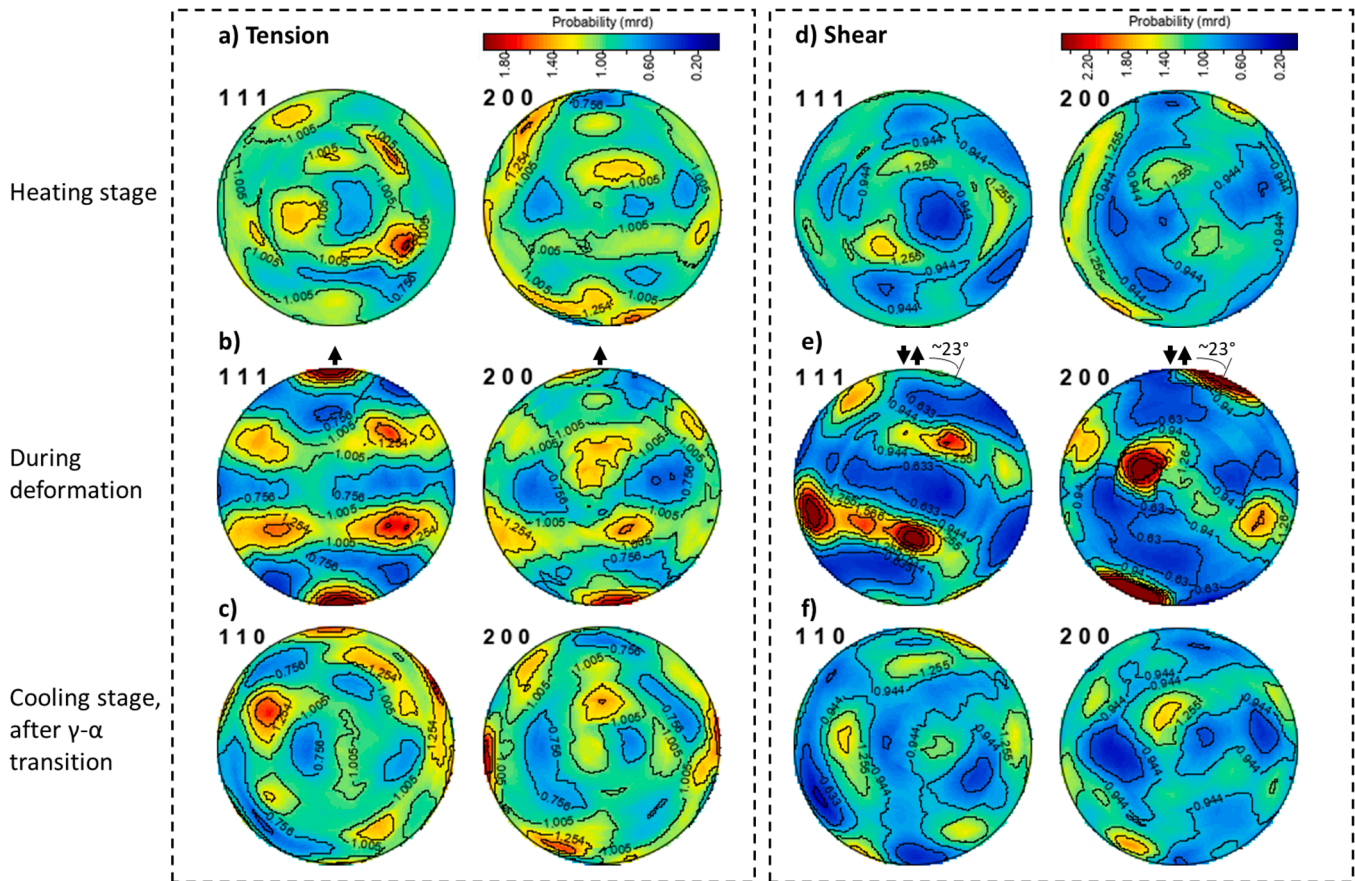
Fig. 7. Pole figures (top) before, (middle) during and (bottom) after the (a-c) tensile and (d-e) shear deformation experiments on 44MnSiV6 at 1300 °C and 1330 °C, respectively. The load direction is vertical (black arrows). The initially untextured samples show preferred orientations during deformation, which dissipate again during cooling and the γ-α phase transition.

and cooling to temperatures below the γ-α phase transition, the orientation appears to be random in the resulting α-Fe structure.

3.5. Lattice strains and evolution of peak widths

Fourier functions were fitted to the (111) and (200) diffraction rings, since the reflections at higher diffraction angles, *e.g.*, the (311) spotty ring, could not be fitted reliably due to low signal-to-noise ratio [50]. The far-field stress-strain response, the evolution of *d* spacing for (111) and the corresponding evolution of relative peak widths for (111) and (200) are shown in Fig. 8. The onset times of DRX, as determined analytically from the stress-strain curves in Section 3.3, are indicated as vertical dashed lines.

Fig. 8(a, b, c) shows for explication the macro-stress measured by the ETMT in all three experiments over time in blue, with the actuator position in black. The corresponding lattice strain in the (111) plane along the loading and transverse axis is shown in Fig. 8(d, e and f) respectively. The lattice strains were determined by obtaining *d* spacing from the Fourier function fit and the *d*-spacings just before deformation were used to calculate the strains. The elastic lattice strains measured on the (111) peak are coloured red in the tensile direction, whilst the strains in the transverse direction are blue. The uncertainties are associated with the spottiness of collected diffraction patterns and estimated from azimuth angles, as detailed in reference [25,51].

The evolution of lattice strains and relative changes in full-width half maximum (FWHM) during deformation in E1, E2 and E3 are shown in Fig. 8. The macroscopic stress and relative cross-head displacement as a function of time for E1 are shown in Fig. 8(a). The corresponding lattice strains (for (111), Fig. 8(d)) and the change in dislocation density is

observed by monitoring relative change in FWHM for (111) and (200) crystallographic plane, shown in Fig. 8(g). The lattice strains along loading axis (North-South in a diffraction ring) and along transverse axis (East-West in the diffraction ring) are obtained by averaging over a 5° azimuth. The strains along the transverse direction are found to be compressive throughout the deformation during E1 and in the loading direction they are tensile over the entire deformation. In the transverse direction, the strain initially observed during far-field elastic strain is −0.004 which recovers to −0.001 during plastic deformation. However, no such large strain reversals are observed along the loading direction, they remain tensile throughout the deformation, Fig. 8(d). There is a step drop of 0.001 observed at ≈0.025 s during the deformation which coincides with the start of DRX (as depicted by vertical dashed line). This clearly indicates that the load partitioning along the loading direction plays a significant role during deformation in E1. This step drop in strain along (111) recovers gradually between 0.025 and 0.05 s during deformation, increasing back to 0.005 and remaining at that level for the rest of the deformation.

In the case of E2, (Fig. 8(b, e and h)), the (111) lattice strains replicate the arc-shaped macro-stress curve in the transverse direction. The maximum strain observed in this case is of the same level as in E1 but there are no sharp changes, rather a shallow wave-like increase in strain is seen with a maxima at 0.04 s and then a plateau during necking up until failure. In the transverse direction, the changes observed are very subtle and shallow from the start of plastic deformation. The strains in this case are compressive initially like in E1, but reaching only up to −0.001 followed by a gradual rise to tensile 0.001 at the start of DRX and then dropping back to −0.001 over time as the deformation progresses and remains at that level during necking until failure.
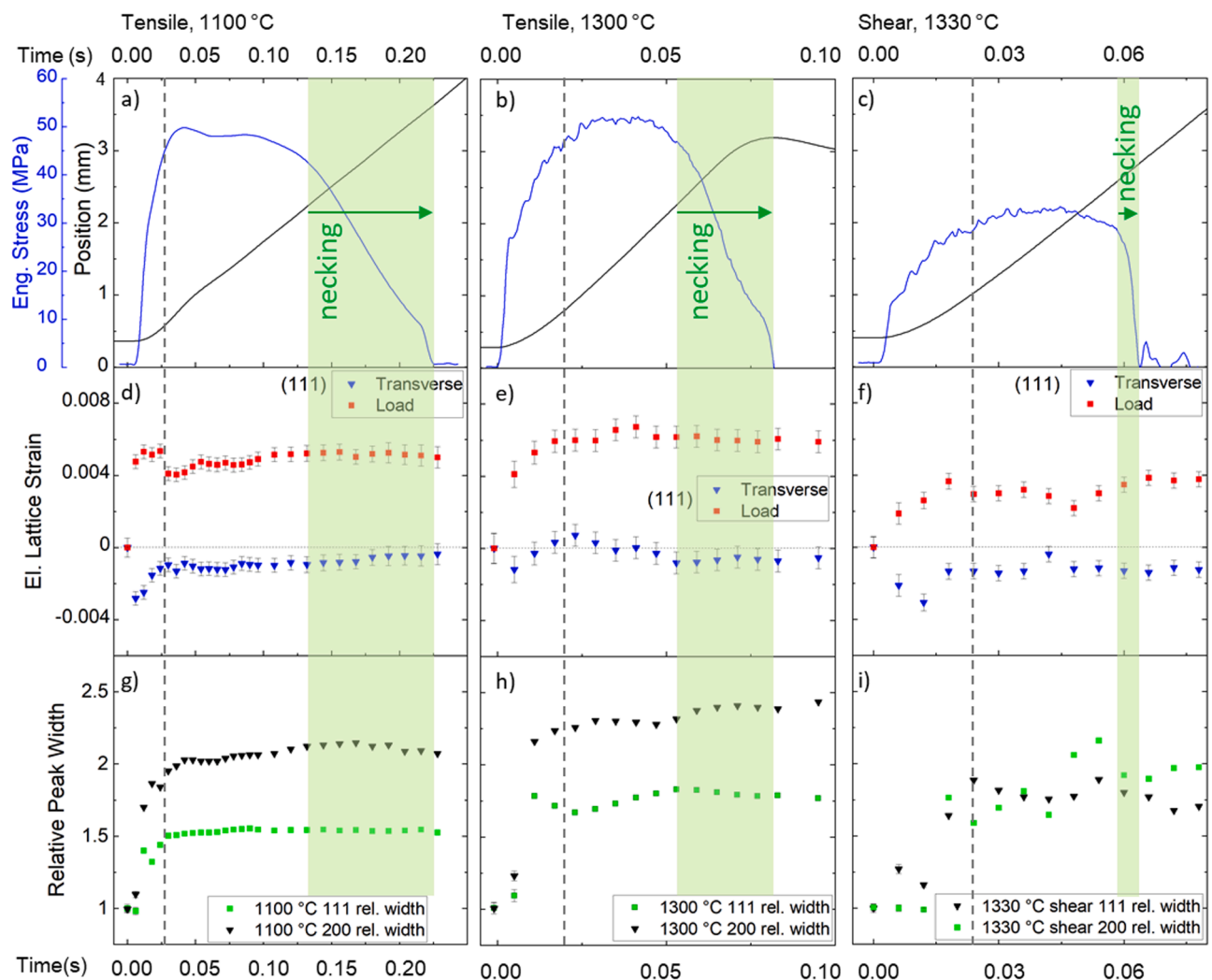
Fig. 8. (a-c) Macro-stress from ETMT, the strain is estimated from crosshead displacement. (d-f) Elastic lattice strains determined from the (111) diffraction peak (middle) in load direction (red) and transverse direction (blue), and (g-i) the relative peak width of the (111) and (200) peaks during deformation on 44MnSiV6 in (a, d, g) tension at 1100 °C and 3 s^{-1}, E1, (b, e, h) tension at 1300 °C and 9 s^{-1}, E2, (c, f, i) shear at 1330 °C and 9 s^{-1}, E3. The error bars of only the first three data points in (g, h, i) are shown to avoid confusion between overlapping data points. The points of DRX initiation derived from the stress-strain data are drawn as vertical dashed lines. The time during which the specimens deformed by localised necking is indicated in green.

The relative change in FWHM is crucial in understanding the evolution and role of dislocations during deformation. In the case of E1 (Fig. 8(g)), the dislocation density accumulated on the (200) plane seems to be much higher than in the (111) plane. At the start of plastic deformation, the relative peak widths (or dislocation density) increase for both planes, followed by plateauing with the start of DRX. The higher temperature in the case of E2 seems to increase the dislocation nucleation and activity, as evident from the relative FWHM in Fig. 8(h), for both (200) and (111) the FWHM are higher than in E1. Like in the case of E1, the dislocation density on (200) is higher than in (111) all throughout the deformation. There is a gradual increase in dislocation density along (200) in E2 followed by a further increase and then plateauing during the necking stage. There is a maxima in relative FWHM observed for (111) just before the start of DRX then a drop, minima of which coincides with the estimated DRX. The dislocation density increases further with deformation and then plateaus during the final stage of deformation.

These observations of lattice strains and dislocation activity indicate that during high-temperature high strain rate tensile deformation, the DRX is either triggered by load partitioning on specific FCC crystallographic planes or its initiation is associated with nucleation and activity of dislocations on specific crystallographic planes.

In Fig. 8(c, f and i), during high-temperature shear deformation, E3, the strain on (111) planes show similar trends as those observed in E1 and E2. That is, the (111) plane along the transverse axis is in compression throughout and along the loading direction they are in tension throughout. Just before the start of DRX, the (111) lattice strain along the loading direction peaks at about 0.004 and about −0.035 along the transverse direction. After DRX, there is a shallow step and a gradual reversal in strains, reaching about the same strain along the transverse direction and about −0.002 along the loading direction. The relative change in FWHM is different in shear mode than those observed in tensile mode. The dislocation density increase and changes in deformation show similar trends on both planes, and the peak density observed is of the same level as those observed in (111) in E1 and E2. Keeping this difference in dislocation activity in tension and shear at 1300 °C in view, we explore the lattice strains along the loading direction as a function of far-field stress, Fig. 9. The diffraction elastic constants for (111) and (200) along tension are found to be ~9 and ~6 GPa respectively. The strains during E2 (Fig. 9(a)) are in tension for (111) and compression for (200), the drop in strain on (200) at 30 MPa coincides with the macroscopic yielding, which indicates that the load partitioning on (200) for triggering plastic deformation. This is also the case during shear mode in E3 where the load partitioning on (200) is
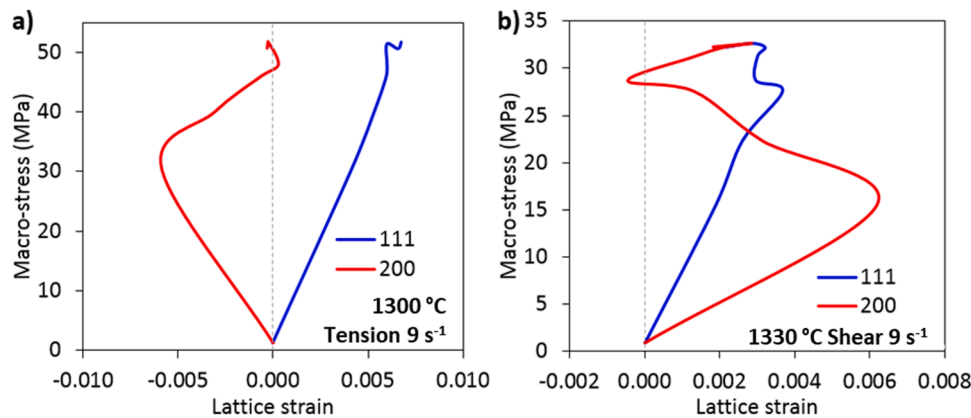
Fig. 9. The evolution lattice strains along the loading direction as a function of far-field stress in (111) and (200) crystal planes during (a) E2 and (b) E3 experiments.

associated with yielding at 15 MPa. It also revealed that the lattice strain on (200) at high temperature can behave differently from that at room temperature with relatively much lower dislocation mobility [52].

These observations indicate that the dislocation activity and the load partitioning on (200) are equally essential for dynamic recrystallisation in tensile and shear deformation of Fe FCC crystals at temperatures exceeding 1300 °C. On the contrary, at temperatures in the vicinity of 1100 °C, the partitioning of load along the loading direction in (111) plays a key role.

4. Conclusions

Using *in situ* synchrotron X-ray powder diffraction experiments, the deformation micro-mechanisms of a microalloyed steel were investigated at high strain rates of 3 s⁻¹ to 9 s⁻¹ in tensile and shear mode at 1100 °C and 1330 °C, exceeding those of common forging regimes. These investigations were carried out to explore the micromechanics of deformation of Fe FCC phases in a near solidus high-strain rate (NSHSR) processing regime which is being extensively explored for near net shape bulk production in various industrial sectors.

It was found that the grains grow rapidly during heating leading to the formation of large grains which undergo dynamic recrystallisation (DRX) during deformation at high strains in both tensile and shear modes. The critical conditions in which DRX occurs are extensively examined by systematically observing the Debye-Scherrer patterns. These events are correlated with the lattice strains, and dislocation density on crystallographic planes, in particular (111) and (200). It has been established that during high-temperature high strain rate tensile deformation, the DRX is triggered by load partitioning on specific FCC crystallographic planes, on (111) at 1100 °C. At 1300 °C, the plastic deformation and DRX are directly associated with load partitioning and dislocation density on the (200) crystallographic plane. The key stages during deformation in all three experiments, such as yielding, plastic deformation, dynamic recrystallisation and necking have been systematically correlated with the evolution of lattice strains and dislocation activity. The broad perspectives presented here can be directly used in refining some of the existing forging and high temperature high strain rate deformation models for steels forged in the austenitic phase regime and for other non ferrous FCC alloys. Moreover, the mechanisms revealed here can contribute to enabling widespread industrial adaptation of this time- and resource-efficient technique and further advancing forming techniques.

CRediT authorship contribution statement

Kai Zhang: Writing – review & editing, Writing – original draft, Software, Methodology, Investigation, Formal analysis, Conceptualization. **Tim Wigger:** Writing – review & editing, Methodology,

Investigation, Data curation, Conceptualization. **Rosa Pineda:** Investigation, Data curation. **Simon A. Hunt:** Writing – review & editing, Software, Investigation, Formal analysis. **Ben Thomas:** Investigation, Data curation. **Thomas Kwok:** Investigation. **David Dye:** Writing – review & editing, Investigation. **Gorka Plata:** Writing – review & editing, Investigation. **Jokin Lozares:** Writing – review & editing, Investigation. **Inaki Hurtado:** Writing – review & editing, Investigation. **Stefan Michalik:** Writing – review & editing, Formal analysis, Data curation. **Michael Preuss:** Writing – review & editing, Investigation. **Peter D. Lee:** Writing – review & editing, Supervision, Resources, Project administration, Methodology, Investigation, Funding acquisition, Formal analysis, Data curation, Conceptualization. **Mohammed A. Azeem:** Writing – review & editing, Supervision, Resources, Project administration, Methodology, Investigation, Funding acquisition, Formal analysis, Data curation, Conceptualization.

Declaration of competing interest

The authors declare that they have no known competing financial interests or personal relationships that could have appeared to influence the work reported in this paper.

Acknowledgements

Supplementary materials

Supplementary material associated with this article can be found, in the online version, at doi:10.1016/j.actamat.2024.120265.

References

[1] J. Lozares, G. Plata, I. Hurtado, A. Sánchez, I. Loizaga, Near solidus forming (NSF): semi-solid steel forming at high solid content to obtain as-forged properties, Metals (Basel) 10 (2020), https://doi.org/10.3390/met10020198.

[2] G. Plata, Semi-Solid Forging of Steels: New insights Into Material Behaviour Evolution and industrialisation, PhD, 2018, p. 173.

[3] J. Lozares, G. Plata, I. Hurtado, Z. Azpilgain, I. Loizaga, Semisolid forging of 250 automotive spindles of s48c steel, Solid State Phenom 285 (SSP) (2019) 411–416, https://doi.org/10.4028/www.scientific.net/SSP.285.411.

[4] T.N. Baker, Microalloyed steels, Ironmak. Steelmak 43 (2016) 264–307, https://doi.org/10.1179/1743281215Y.0000000063.

[5] H. Karbasian, A.E. Tekkaya, A review on hot stamping, J. Mater. Process. Technol. 210 (2010) 2103–2118, https://doi.org/10.1016/j.jmatprotec.2010.07.019.

[6] C. Haase, O. Kremer, W. Hu, T. Ingendahl, R. Lapovok, D.A. Molodov, Equal-channel angular pressing and annealing of a twinning-induced plasticity steel: microstructure, texture, and mechanical properties, Acta Mater 107 (2016) 239–253, https://doi.org/10.1016/j.actamat.2016.01.056.

[7] M. Nezakat, H. Akhiani, M. Hoseini, J. Szpunar, Effect of thermo-mechanical processing on texture evolution in austenitic stainless steel 316L, Mater. Charact. 98 (2014) 10–17, https://doi.org/10.1016/j.matchar.2014.10.006.

[8] H.J. McQueen, C.A.C. Imbert, Dynamic recrystallization: plasticity enhancing structural development, J. Alloys Compd. 378 (2004) 35–43, https://doi.org/10.1016/j.jallcom.2003.10.067.

[9] G.E. Dieter, H.a. Kuhn, S.L. Semiatin, Handbook of Workability and Process Design, 2003, https://doi.org/10.1361/hwpd2003p232.

[10] T. Sakai, A. Belyakov, R. Kaibyshev, H. Miura, J.J. Jonas, Dynamic and post-dynamic recrystallization under hot, cold and severe plastic deformation conditions, Prog. Mater. Sci. 60 (2014) 130–207, https://doi.org/10.1016/j.pmatsci.2013.09.002.

[11] N.D. Ryan, H.J. McQueen, E. Evangelista, Dynamic recovery and strain hardening in the hot deformation of type 317 stainless steel, Mater. Sci. Eng. 81 (1986) 259–272, https://doi.org/10.1016/0025-5416(86)90267-3.

[12] G. zheng Quan, L. Zhao, T. Chen, Y. Wang, Y. ping Mao, W. quan Lv, J. Zhou, Identification for the optimal working parameters of as-extruded 42CrMo high-strength steel from a large range of strain, strain rate and temperature, Mater. Sci. A. 538 (2012) 364–373, https://doi.org/10.1016/j.msea.2012.01.062.

[13] K.A. Babu, S. Mandal, C.N. Athreya, B. Shakthipriya, V.S. Sarma, Hot deformation characteristics and processing map of a phosphorous modified super austenitic stainless steel, Mater. Des. 115 (2017) 262–275, https://doi.org/10.1016/j.matdes.2016.11.054.

[14] H. Ji, J. Liu, B. Wang, X. Tang, J. Lin, Y. Huo, Microstructure evolution and constitutive equations for the high-temperature deformation of 5Cr21Mn9Ni4N heat-resistant steel, J. Alloys Compd. 693 (2017) 674–687, https://doi.org/10.1016/j.jallcom.2016.09.230.

[15] K.D. Liss, T. Schmoelzer, K. Yan, M. Reid, M. Peel, R. Dippenaar, H. Clemens, In situ study of dynamic recrystallization and hot deformation behavior of a multiphase titanium aluminide alloy, J. Appl. Phys. (2009) 106, https://doi.org/10.1063/1.3266177.

[16] K.D. Liss, U. Garbe, H. Li, T. Schambron, J.D. Almer, K. Yan, In situ observation of dynamic recrystallization in the bulk of zirconium alloy, Adv. Eng. Mater. 11 (2009) 637–640, https://doi.org/10.1002/adem.200900094.

[17] S.L. Raghunathan, M.A. Azeem, D. Collins, D. Dye, In situ observation of individual variant transformations in polycrystalline NiTi, Scr. Mater. 59 (2008) 1059–1062, https://doi.org/10.1016/j.scriptamat.2008.07.014.

[18] M.A. Azeem, D. Dye, Lattice instability during the martensitic transformation in the high temperature shape memory alloy Zr(Cu0.5Co0.25Ni0.25), J. Alloys Compd. 618 (2015) 469–474, https://doi.org/10.1016/j.jallcom.2014.08.141.

[19] M.A. Azeem, D. Dye, In situ evaluation of the transformation behaviour of NiTi-based high temperature shape memory alloys, Intermetallics 46 (2014) 222–230, https://doi.org/10.1016/j.intermet.2013.11.009.

[20] K.D. Liss, K. Yan, Thermo-mechanical processing in a synchrotron beam, Mater. Sci. Eng. A. 528 (2010) 11–27, https://doi.org/10.1016/j.msea.2010.06.017.

[21] D. Tolnai, R.H. Buzolin, F. D'Elia, T. Subroto, S. Gavras, A. Stark, N. Schell, K. U. Kainer, N. Hort, The Role of Zn on the elevated temperature compression behavior of Mg5Nd: an In Situ synchrotron radiation diffraction study, Jom 68 (2016) 3051–3056, https://doi.org/10.1007/s11837-016-2159-8.

[22] K. Yan, D.G. Carr, M.D. Callaghan, K.D. Liss, H. Li, Deformation mechanisms of twinning-induced plasticity steels: in situ synchrotron characterization and modeling, Scr. Mater. 62 (2010) 246–249, https://doi.org/10.1016/j.scriptamat.2009.11.008.

[23] Š. Dubravka, T. Donath, O. Magdysyuk, J. Bednarcik, D. Šišak Jung, T. Donath, O. Magdysyuk, J. Bednarcik, High-energy X-ray applications: current status and new opportunities, Powder Diffr 32 (2017) S22–S27, https://doi.org/10.1017/S0885715617001191.

[24] M. Rowson, C.J. Bennett, M.A. Azeem, O. Magdysyuk, J. Rouse, R. Lye, J. Davies, S. Bray, P.D. Lee, Observation of microstructure evolution during inertia friction welding using in-situ synchrotron X-ray diffraction, J. Synchrotron Radiat. 28 (2021) 790–803, https://doi.org/10.1107/S1600577521001569.

[25] Y. Chen, S.J. Clark, D.M. Collins, S. Marussi, S.A. Hunt, D.M. Fenech, T. Connolley, R.C. Atwood, O.V. Magdysyuk, G.J. Baxter, M.A. Jones, C.L.A. Leung, P.D. Lee, Correlative synchrotron X-ray imaging and diffraction of directed energy deposition additive manufacturing, Acta Mater 209 (2021), https://doi.org/10.1016/j.actamat.2021.116777.

[26] G. Plata, J. Lozares, I. Hurtado, Z. Azpilgain, Z. Idoyaga, Semisolid forming of 44MnSiV6 microalloyed steel, in: AIP Conf. Proc, 2018, p. 1960, https://doi.org/10.1063/1.5034990.

[27] W.U. Mirihanage, J.D. Robson, S. Mishra, P. Hidalgo-Manrique, J.Q. da Fonseca, C. S. Daniel, P.B. Prangnell, S. Michalik, O.V. Magdysyuk, T. Connolley, M. Drakopoulos, Direct observation of the dynamic evolution of precipitates in aluminium alloy 7021 at high strain rates via high energy synchrotron X-rays, Acta Mater 205 (2021) 116532, https://doi.org/10.1016/j.actamat.2020.116532.

[28] B. Roebuck, M. Brooks, A. Pearce, Good Practice Guide For Miniature ETMT Tests, Good Pract. Guid. No.137, 2016.

[29] Y.T. Tang, C. Schwalbe, M. Futoma, B. Roebuck, S. Utada, R.C. Reed, A comparative study of high temperature tensile and creep testing between standard and miniature specimens: applicability and limits, Metall. Mater. Trans. A Phys. Metall. Mater. Sci. 54 (2023) 1568–1581, https://doi.org/10.1007/s11661-022-06869-x.

[30] M. Drakopoulos, T. Connolley, C. Reinhard, R. Atwood, O. Magdysyuk, N. Vo, M. Hart, L. Connor, B. Humphreys, G. Howell, S. Davies, T. Hill, G. Wilkin, U. Pedersen, A. Foster, N. De Maio, M. Basham, F. Yuan, K. Wanelik, I12: the joint engineering, environment and processing (JEEP) beamline at diamond light source, J. Synchrotron Radiat. 22 (2015) 828–838, https://doi.org/10.1107/S1600577515003513.

[31] M. Basham, J. Filik, M.T. Wharmby, P.C.Y. Chang, B. El Kassaby, M. Gerring, J. Aishima, K. Levik, B.C.A. Pulford, I. Sikharulidze, D. Sneddon, M. Webber, S. S. Dhesi, F. Maccherozzi, O. Svensson, S. Brockhauser, G. Náray, A.W. Ashton, Data analysis WorkbeNch (DAWN), J. Synchrotron Radiat 22 (2015) 853–858, https://doi.org/10.1107/S1600577515002283.

[32] J. Filik, A.W. Ashton, P.C.Y. Chang, P.A. Chater, S.J. Day, M. Drakopoulos, M. W. Gerring, M.L. Hart, O.V. Magdysyuk, S. Michalik, A. Smith, C.C. Tang, N. J. Terrill, M.T. Wharmby, H. Wilhelm, Processing two-dimensional X-ray diffraction and small-angle scattering data in DAWN 2, J. Appl. Crystallogr. 50 (2017) 959–966, https://doi.org/10.1107/S1600576717004708.

[33] L. Lutterotti, R. Vasin, H.R. Wenk, Rietveld texture analysis from synchrotron diffraction images. I. Calibration and basic analysis, Powder Diffr 29 (2014) 76–84, https://doi.org/10.1017/S0885715613001346.

[34] H.R. Wenk, S. Matthies, J. Donovan, D. Chateigner, BEARTEX: a Windows-based program system for quantitative texture analysis, J. Appl. Crystallogr. 31 (1998) 262–269, https://doi.org/10.1107/S002188989700811X.

[35] C.S. Daniel, X. Zeng, Š. Michalik, S.A. Hunt, J.Q. da Fonseca, Application of a new method for accurate determination of α and β texture in Ti-6Al-4V from synchrotron diffraction intensities, Mater. Charact. 199 (2023) 112769, https://doi.org/10.1016/j.matchar.2023.112769.

[36] T. Ungár, S. Ott, P.G. Sanders, A. Borbély, J.R. Weertman, Dislocations, grain size and planar faults in nanostructured copper determined by high resolution X-ray diffraction and a new procedure of peak profile analysis, Acta Mater 46 (1998) 3693–3699, https://doi.org/10.1016/S1359-6454(98)00001-9.

[37] S.J. Lewis, C.E. Truman, Diffraction measurements for evaluating plastic strain in A533B ferritic steel-a feasibility study, J. Phys. D. Appl. Phys. (2010) 43, https://doi.org/10.1088/0022-3727/43/26/265501.

[38] A. Laasraoui, J.J. Jonas, Prediction of steel flow stresses at high temperatures and strain rates, Metall. Trans. A. 22 (1991) 1545–1558, https://doi.org/10.1007/BF02667368.

[39] C. Chauvy, P. Barbéris, F. Montheillet, Dynamic recrystallization of Zircaloy-4 during working within the upper α-range, Mater. Sci. Forum. 467–470 (2004) 1151–1156, https://doi.org/10.4028/www.scientific.net/msf.467-470.1151.

[40] S.K. Pradhan, S. Mandal, C.N. Athreya, K.A. Babu, B. de Boer, V.S. Sarma, Influence of processing parameters on dynamic recrystallization and the associated annealing twin boundary evolution in a nickel base superalloy, Mater. Sci. Eng. A. 700 (2017) 49–58, https://doi.org/10.1016/j.msea.2017.05.109.

[41] G. Quan, Y. Tong, G. Luo, J. Zhou, A characterization of the flow behavior of 42CrMo steel, Comput. Mater. Sci. 50 (2010) 167–171, https://doi.org/10.1016/j.commatsci.2010.07.021.

[42] M. Shaban, B. Eghbali, Determination of critical conditions for dynamic recrystallization of a microalloyed steel, Mater. Sci. Eng. A. 527 (2010) 4320–4325, https://doi.org/10.1016/j.msea.2010.03.086.

[43] Y.Q. Cheng, H. Zhang, Z.H. Chen, K.F. Xian, Flow stress equation of AZ31 magnesium alloy sheet during warm tensile deformation, J. Mater. Process. Technol. 208 (2008) 29–34, https://doi.org/10.1016/j.jmatprotec.2007.12.095.

[44] K. Huang, R.E. Logé, A review of dynamic recrystallization phenomena in metallic materials, Mater. Des. 111 (2016) 548–574, https://doi.org/10.1016/j.matdes.2016.09.012.

[45] E.I. Poliak, J.J. Jonas, A one-parameter approach to determining the critical conditions for the initiation of dynamic recrystallization, Acta Mater 44 (1996) 127–136, https://doi.org/10.1016/1359-6454(95)00146-7.

[46] P.A. Manohar, D.P. Dunne, T. Chandra, C.R. Killmore, Grain growth predictions in microalloyed steels, ISIJ Int 36 (1996) 194–200, https://doi.org/10.2355/isijinternational.36.194.

[47] D. Xu, C. Ji, H. Zhao, D. Ju, M. Zhu, A new study on the growth behavior of austenite grains during heating processes, Sci. Rep. 7 (2017) 1–13, https://doi.org/10.1038/s41598-017-04371-8.

[48] X.X. Wang, M. Zhan, P.F. Gao, P.Y. Ma, K. Yang, Y.D. Lei, Z.X. Li, Deformation mode dependent mechanism and kinetics of dynamic recrystallization in hot working of titanium alloy, Mater. Sci. Eng. A. (2020) 772, https://doi.org/10.1016/j.msea.2019.138804.

[49] B.C. De Cooman, Y. Estrin, S.K. Kim, Twinning-induced plasticity (TWIP) steels, Acta Mater 142 (2018) 283–362, https://doi.org/10.1016/j.actamat.2017.06.046.

[50] M.R. Daymond, The determination of a continuum mechanics equivalent elastic strain from the analysis of multiple diffraction peaks, J. Appl. Phys. 96 (2004) 4263–4272, https://doi.org/10.1063/1.1794896.

[51] J.R. Taylor, An Introduction to Error Analysis, Univ. Sci. Books, Sausalito, Calif, 1997, p. 327.

[52] B. Clausen, T. Lorentzen, T. Leffers, Self-consistent modelling of the plastic deformation of F.C.C. polycrstals and its implications for diffraction measurements of internal stresses, Acta Mater 46 (1998) 3087–3098, https://doi.org/10.1016/S1359-6454(98)00014-7.